Spreading of a deep-ocean tracer in a suite of Eulerian and Lagrangian simulations

M. Gabriela Escobar-Franco[1], Mathieu Huret[1], Clément Vic[1], Thomas Gorgues[1], Jonathan Gula[1]and Cécile Cathalot[2]

[1]University of Brest, CNRS, Ifremer, IRD, Laboratoire d'Océanographie Physique et Spatiale (LOPS), IUEM, Plouzané, France
[2]University of Brest, Université de Bretagne Sud, CNRS, Ifremer, Geo-Ocean, IUEM, Plouzané, France

Key Points:

- Kilometer-scale seafloor topography is essential to catalyze submesoscale turbulence over a mid-ocean ridge
- Submesoscale turbulence is instrumental in the spreading of a deep-ocean tracer but tides have limited effects
- Lagrangian and Eulerian frameworks lead to similar horizontal spreading pathways on long time scales

Corresponding author: Gabriela Escobar, maria-gabriela.escobarfranco@univ-brest.fr

Abstract

Hydrothermal vents are important sources of biogeochemical constituents with a global relevance, like iron. The fate of these elements is poorly constrained, both by the physical mechanisms of transport and mixing, and by the geochemical speciation processes. Here we set up a regional simulation of the ocean circulation that resolves submesoscale and tidal processes around the Trans-Atlantic Geotraverse (TAG) hydrothermal vent to investigate how the small scales of the dynamics impact the dispersal of a hydrothermal plume. A passive Eulerian tracer is continuously released at TAG and spreads over 260 days. We design sensitivity experiments to isolate key forcing mechanisms: a simulation without tides, a simulation with a bathymetry that is smoothed to remove kilometer-scale features, and a simulation with Lagrangian particles to be compared to the Eulerian framework. We find that the kilometer-scale seafloor topography is essential to drive submesoscale instabilities and generate submesoscale eddies that capture seafloor material and transport it off the ridge, increasing dramatically the horizontal spreading as compared to the smooth-bathymetry simulation. Tides are found to increase vertical diffusivity above the ridge, but their impact on the horizontal dispersal is negligible. Eulerian and Lagrangian experiments lead to very similar horizontal dispersal pathways, although the vertical spreading is much reduced in the Lagrangian simulation, which is explained by the lack of an explicit representation of mixing processes.

Plain Language Summary

Ocean dynamics at kilometer scales have been shown to strongly impact the spreading of material at the ocean surface, but their impact in the deep ocean remains understudied. We designed and ran numerical experiments to resolve the fine-scale ocean currents at depth and their interaction with the seafloor, to study their impact on the spreading of material from hydrothermal vents on the Mid-Atlantic Ridge. We find that the seafloor features at kilometer scales are crucial to generate eddies that transport material off the Ridge, but tides have a limited impact. The seafloor and dynamical small scales are not included in global models, which likely leads to a misrepresentation of the pathways and fate of hydrothermal biogeochemical compounds.

1 Introduction

Hydrothermal vents, mostly located over mid-ocean ridges, are important sources of biogeochemical constituents, and host benthic and pelagic populations (Lutz & Kennish, 1993; Baker & German, 2004; Martin & Russell, 2007; Matabos et al., 2025). Over the past decades, there has been increased evidence for basin-scale spreading of hydrothermal plumes and their biogeochemical constituents (Nishioka et al., 2013; Resing et al., 2015; Fitzsimmons et al., 2017). Some of these constituents, like iron, escape ultimately from the deep ocean, from which they subsequently influence the upper ocean and thus significantly contribute to global biogeochemical cycles (Tagliabue et al., 2010; Tagliabue & Resing, 2016; Früh-Green et al., 2022). The distribution of these hydrothermal constituents is influenced by both physical processes and geochemical speciation processes as they are released and exported up to thousands of kilometers away from their source. Nevertheless, many unknowns remain on the short- and long-term fate of these constituents. Indeed, it is difficult to disentangle the impacts of multi-scale oceanic transport and mixing from poorly constrained biogeochemical processes. Yet, it is crucial to estimate how, how far, and in what proportion hydrothermal plumes disperse from their sources, to assess their influence and impact on the upper-ocean biological activity and global carbon cycle (Tagliabue et al., 2010; Tagliabue & Resing, 2016; Ardyna et al., 2019; González-Santana et al., 2020).

Physics-biogeochemical coupling is fairly well documented in the surface layer of the ocean. For example, mesoscale eddies ($\mathcal{O}$(10-100 km)) can trap plankton and nutrients and transport them through ocean basins (Gaube et al., 2014). Submesoscale dynamics

($\mathcal{O}$(0.1-10 km)) drive vertical exchanges near the surface, critically impact biogeochemical cycles, and shape ecosystems (Klein & Lapeyre, 2009; Lévy et al., 2018, 2024). More recent research has shown that tidally-driven mixing can impact vertical fluxes of, e.g., nutrients, in the surface layers (Tuerena et al., 2019). In the deep ocean, the physical processes that impact the transport and mixing of tracers are less clear, although there is evidence for the existence of mesoscale and submesoscale eddies (Frenger et al., 2018; McCoy et al., 2020) and locally enhanced tidally-driven mixing over rough seafloor topography (Waterhouse et al., 2014). Specifically, there is scarce evidence for an impact of small-scale ocean currents (submesoscales and tidal) on the deep-ocean biogeochemical fluxes in hydrothermal environments (Fujioka et al., 1997; Furushima & Yamamoto, 2014; Cuvelier et al., 2017; Sarrazin et al., 2020).

Some recent studies focused on the physical mechanisms at play in the dispersal of hydrothermal material using hydrostatic primitive-equation models, which solve the largest scales of the oceanic circulation. Using global models with grid scales of $\mathcal{O}$(10) km, hydrothermal plumes and their constituents were represented as Eulerian tracers (e.g., Tagliabue et al., 2022), while they were represented as Lagrangian particles using regional models with grid scales of $\mathcal{O}$(1) km (e.g., Breusing et al., 2016; Vic et al., 2018; Tagliabue et al., 2022). Lagrangian simulations are more cost-effective as they can be run offline, i.e., using 3-dimensional currents to transport particles. A potentially significant limit of Lagrangian methods is that they intrinsically lack vertical mixing, unless a parameterization built on stochastic processes is specifically included to represent it (van Sebille et al., 2018). Within the surface ocean, Lagrangian models have proven to be useful to simulate tracer spreading in mesoscale-resolving simulations. However, they tend to underestimate vertical spreading as compared to Eulerian models (Wagner et al., 2019). Using submesoscale-resolving models that include tides, one would expect vertical mixing to be largely enhanced as compared to coarser models, both due to emerging submesoscale instabilities and tidal mixing (Gula et al., 2016; Thakur et al., 2022; Mashayek et al., 2024; Ruan et al., 2025). This is especially true near the ocean floor where frictional effects drive mixing processes, and in the adjacent $\mathcal{O}$(100)-m vertical layer where tidally-driven mixing is prominent (Winters, 2015; van Haren et al., 2017; Naveira Garabato et al., 2025). Yet, we still lack a comparison of Lagrangian and Eulerian models in the deep ocean.

Here, as part of the LifeDeeper project (Cambon & Pelleter, 2025), we aim to shed light on the fate of the hydrothermal plume emitted at the Trans-Atlantic Geotraverse (TAG) hydrothermal site. TAG is an active sulfide mound located on the Mid-Atlantic Ridge (MAR) around 26°N at 3620 m depth, which has received extensive attention over the past decades (Rona et al., 1986; Pelleter et al., 2024). Several observational plans were designed to investigate the vent field and the geochemical characterization of the trace metal hydrothermal plume (Fouquet et al., 2017; González-Santana et al., 2020). In this study, we use a numerical modeling approach at high horizontal and vertical resolutions to represent the deep-ocean fine-scale dynamics and its impacts on tracer dispersal as accurately as possible.

We focus on the dispersal of a passive tracer within the hydrothermal plume, considered here only once it has reached its neutrally-buoyant altitude. The initial, ascending, stage of the plume dynamics feature large vertical velocity, which cannot be simulated with a hydrostatic model and at the resolution we consider (Lemaréchal et al., 2025). The passive tracer could be identified as helium, a chemically inert gas considered as a conservative tracer and which isotopic composition in ^{3}He is often used as a marker of hydrothermal plumes (Jean-Baptiste et al., 1991; Lupton et al., 1998; Lupton, 1998). The fate of such tracer is hypothesized to be solely constrained by the physics. Our goal is twofold. First, we aim to investigate the specific roles of tides and kilometer-scale seafloor topography in the dispersal of a passive Eulerian tracer of hydrothermal origin. Second, we aim to benchmark the widely used Lagrangian approach with an Eulerian simulation specifically designed to study the deep ocean. To investigate the spreading of the TAG hydrothermal

plume material, we examine the underlying physical processes. A reference experiment includes realistic forcing, i.e., a high-resolution bathymetry and high-frequency atmospheric and tidal forcing. We then test the sensitivity of the dynamics to tides by switching them off in a twin experiment, and to small-scale seafloor topography by smoothing the original bathymetry in a third experiment – the resulting bathymetry is representative of that used in global climate models. The passive tracer is continuously released at TAG with an initial distribution based on observations of helium. In addition, a Lagrangian experiment is carried out using a distribution of particles that mimics the Eulerian tracer distribution.

The paper is organized as follows. Section 2 describes the methods, model and data used in the analyses. Section 3 presents how small-scale seafloor topography and tides control the dynamics. Section 4 demonstrates their impacts on the spreading of a passive Eulerian tracer and of Lagrangian particles. Results are summarized and discussed in Section 5.

2 Data and Methods

2.1 Numerical Setup

We use the hydrostatic version of the Coastal and Regional Ocean Community Model (CROCO, Auclair et al., 2025), based on the Regional Ocean Modelling System (ROMS, Shchepetkin & McWilliams, 2005). CROCO solves the primitive equations on an orthogonal curvilinear grid with terrain-following coordinates (σ-levels). Parameters and numerical options common to the set of simulations are given in Section 2.1.1, and details specific to the simulations are given in Section 2.1.2. The Lagrangian experiment is described in Section 2.1.3.

2.1.1 Background

The 600 km × 500 km model domain is centered on the TAG hydrothermal vent site (Figure 1a). The horizontal grid spacing is 1 km and the grid has 150 vertical levels, with stretching parameters $\theta_s = 3$, $\theta_b = 3$ and $h_c = 300$ m. This corresponds to a vertical grid spacing of ≈15-20 m near the bottom, ≈40 m in the middle of the water column, and ≈2 m near the surface. The large number of vertical levels at such horizontal resolution is necessary to avoid numerical instabilities in boundary layers – the grid satisfies the criterion proposed in Ménesguen et al. (2025) to avoid baroclinic instability of the computational kind (not shown) – and to accurately represent the vertical structure of the hydrothermal plume. The model bathymetry is based on the Shuttle Radar Topography Mission dataset at 30-sec resolution (SRTM30_PLUS, Becker et al., 2009). Additional smoothing is performed on the original topography to minimize pressure gradient errors and limit spurious numerical mixing; this is detailed below. Atmospheric forcing is provided at hourly resolution by the Climate Forecast System Reanalysis (CFSR, Saha et al., 2010). Initial and lateral boundary conditions are provided by a simulation covering the North Atlantic Ocean with a horizontal grid spacing of 3 km (GIGATL3, Gula et al., 2021). The grid refinement coefficient of 3 ensures smooth dynamical transitions at boundaries (Debreu & Blayo, 2008). The simulations are run for year 2009, from which the first three months were considered a spin-up stage allowing the model to stabilize the physics from the parent simulation (see kinetic energy time series in Figure S1 in Supporting Information), hence were discarded from the analyses.

In all simulations, mixing is parameterised using the K-profile parameterization scheme (KPP, Large et al., 1994). For active tracers, we use the horizontal advection scheme RSUP5 (split and rotated 5th-order upstream biased advection scheme, Lemarié, Debreu, et al., 2012) and the vertical advection scheme SPLINES. For passive tracers, we use WENO5 (5th-order weighted essentially non-oscillatory scheme, Jiang & Shu, 1996) both for horizontal and vertical advection schemes, to avoid negative concentrations. To simulate the Eulerian tracers, and in anticipation of a future study of iron dispersal, we use the PISCES

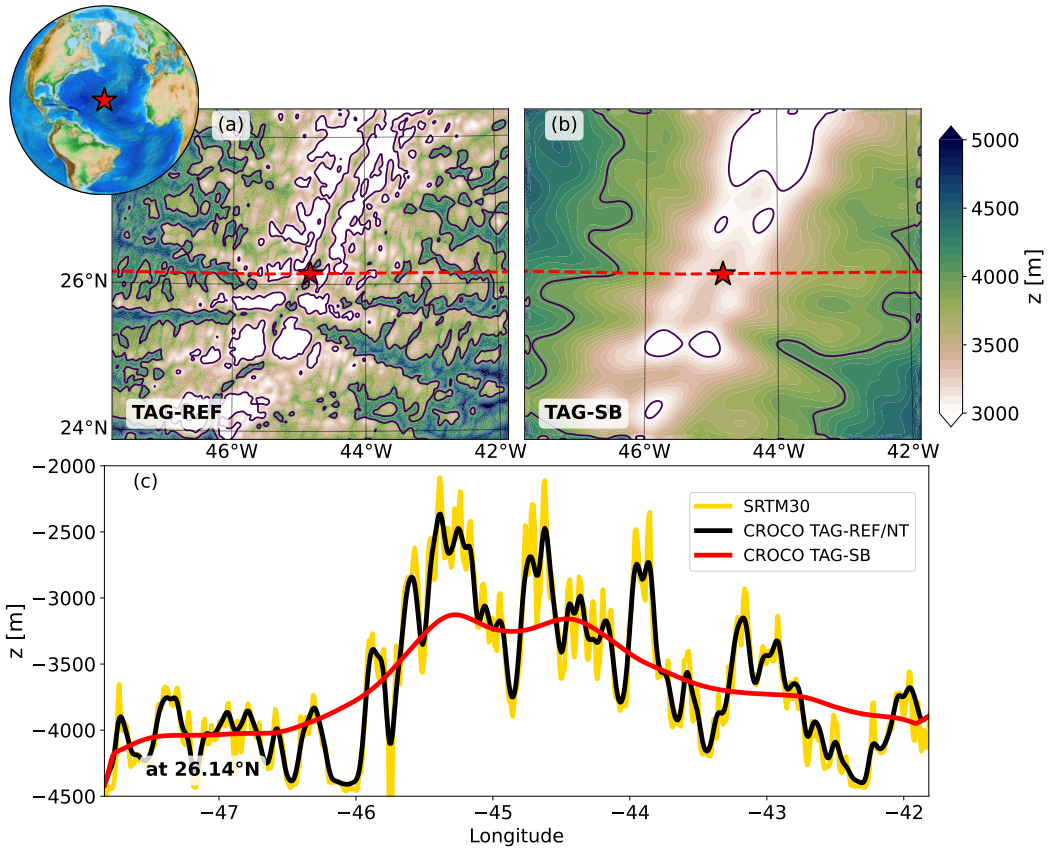

Figure 1. Model domain and bathymetry, centered at the TAG site for the (a) TAG-REF and TAG-NT simulations, and the (b) TAG-SB simulation. Black contours are isobaths 3000 and 4000 m. TAG is shown by the red star. (c) Zonal section of bathymetry at 26.14°N through TAG, along the dashed red line in (a) and (b). The original SRTM30_PLUS bathymetry is shown in gold, the bathymetry used in TAG-REF and TAG-NT simulations is shown in black, and the bathymetry used in TAG-SB is shown in red.

biogeochemical model framework (Aumont et al., 2015), coupled to the CROCO simulation. Initial and boundary conditions for PISCES variables were derived from the World Ocean Atlas 2023 monthly climatology dataset (Garcia et al., 2024). To simulate the dispersal of a passive (inert, non-reactive) tracer, we incorporated a new tracer – helium-3 (^3He) – into PISCES. The tracer initialization is based on measurements collected at the TAG site and presented in Section 2.3.

2.1.2 Set of Simulations

The reference simulation, TAG-REF, includes small-scale topography and tidal forcing, resolving the widest range of processes. Original bathymetry from SRTM30_PLUS is smoothed with a Gaussian filter with a half-width of 6 grid points to avoid pressure gradient errors. The maximum steepness ratio of the grid is $r_0 = 0.049$, well below the typically recommended threshold of 0.2 (Lemarié, Kurian, et al., 2012). TAG-REF bathymetry is shown in Figures 1a and 1c. Although the smoothing removes some kilometer-scale crests and troughs, the structure of the ridge with its inner valley is well preserved. Tidal forcing is embedded within the lateral boundary forcing. The parent simulation is forced by barotropic

tides (8 principal constituents) and spontaneously generates internal tides. Boundary forcing is provided at an hourly frequency to ensure that tidal dynamics are accurately represented.

The no-tide simulation, TAG-NT, is essentially the same as TAG-REF, with the exception that lateral boundaries are forced by a parent simulation that does not include tides. Boundary forcing is provided with a frequency of 12 h.

The smooth-bathymetry simulation, TAG-SB, has a bathymetry that is smoothed with a Gaussian filter with a half-width of 48 grid points, preserving only the largest ridge shape and providing a very crude representation of the inner valley (Figures 1b and 1c). This bathymetry resembles those used in global climate models (not shown). The lateral boundary forcing is the same as for TAG-NT – tidal processes are not included.

In the three simulations, the tracer is continuously injected by forcing a vertical profile of its concentration at a single grid point (26.137°N, 44.826°W). The simulations are hydrostatic and do not resolve the ascending phase of the plume (Lemaréchal et al., 2025). Hence, we inject the tracer as if it were already within the neutrally-buoyant plume. The vertical distribution is analytical and based on observations (Section 2.3). It follows a Gaussian distribution with a maximum concentration of 2.62×10^{-15} mol kg^{-1} at 3250 m depth, which corresponds to 412 m above the seafloor, and has a standard deviation of 50 m.

2.1.3 Lagrangian particle-tracking experimental setup

To compare the trajectories of the passive tracer between the Eulerian and Lagrangian approaches, we performed a Lagrangian experiment, TAG-LAG, using the particle-tracking model Pyticles (Gula et al., 2014). The hourly 3-dimensional velocity field from the TAG-REF simulation was used to advect particles. Every hour, 100 synthetic particles were released at the same grid points and with the same vertical Gaussian distribution used for the tracer in TAG-REF. The particles are passively transported by the 3-dimensional flow. Their trajectories were computed using a fourth-order Runge–Kutta scheme, with the velocity field linearly interpolated in space and time.

2.2 In Situ Estimate of Diapycnal Mixing

In order to assess the realism of our modeled diffusivity profiles, we compare them to in situ estimates of diffusivity. Microstructure measurements of velocity shear provide the best data to estimate the rate of kinetic energy dissipation ε (e.g., Waterhouse et al., 2014). ε is then used to estimate diffusivity $\kappa_{obs} = \Gamma\varepsilon/N^2$ (Osborn, 1980), with N^2 the buoyancy frequency and $\Gamma = 0.2$ (Gregg et al., 2018).

We used microstructure-derived ε and N^2 profiles from the BBTRE (Polzin et al., 1997) and the DoMORE (Clément et al., 2017) datasets localized on the MAR in the south Atlantic subtropical gyre. Although this region does not overlap with our simulated domain, these are the closest datasets available, and we expect mixing to be dominated by tidal processes at both sites, with similar intensity, due to the comparable barotropic tidal currents and seafloor topography characteristics (see Figures 2 and 5 in Vic et al., 2019). We selected only profiles which were above the MAR (11-15°W, 20-22°S) in waters shallower than 4500 m to avoid deep fracture zones, which are associated with specific dynamics and energy dissipation (Clément et al., 2017), and are absent from our simulated domain. In total, this selection represents 15 profiles. The original dataset is binned in the vertical in 0.5-dbar bins, and we computed statistics in 50-m bins to smooth out the spatio-temporal variability.

Finally, in order to get an estimate of energy dissipation that is quantitatively representative of the area around TAG, we rescaled the observed diffusivity using an independent estimate of tidally-driven energy dissipation (de Lavergne et al., 2019). In practice, we computed the mean energy dissipation predicted by de Lavergne et al. (2019) in our model

domain (ε_{TAG}) and where the observed diffusivity profiles are taken ($\varepsilon_{BBTRE-DoMORE}$), then we multiplied the observed diffusivity by $\varepsilon_{TAG}/\varepsilon_{BBTRE-DoMORE}$. This ratio is small (0.51) regarding the natural variability of energy dissipation in the ocean, but allows to rescale the observed diffusivity so that it would be more representative of the local tidal dynamics and associated energy dissipation and mixing.

2.3 In Situ Velocity and Helium Data

In order to assess the realism of the modeled currents, we compared them to in-situ measurements of currents during a one-year-long mooring deployment at TAG. Three 300-kHz Acoustic Doppler Current Profilers (ADCPs, manufactured by Teledyne RDI) were deployed from April 2017 to April 2018 (Fouquet et al., 2017). These ADCPs were set up on a single mooring line as follows: an upward-looking ADCP and a downward-looking ADCP at 3240 m depth, and a downward-looking ADCP at 3510 m. They provide velocity measurements in 4-m bins and formed ensembles every 20 min. In the following, we only consider data from the topmost ADCP, averaged over the overall height covered by the measurements. Indeed, we consider that this dataset sits at a height above the seafloor that might not be too impacted by surrounding small-scale bathymetric scales not represented in the model (Figure 1c), so that the hydrodynamical conditions would be comparable to the modeled conditions.

Seawater samples for helium analyses were collected in the water column samples during the Hermine cruise onboard R/V Pourquoi Pas ? from 16 March to 27 April 2017 (Fouquet et al., 2017). Five vertical profiles were performed using a CTD (Conductivity Temperature Depth) system Seabird SBE 911+ mounted on a Rosette carousel sampler, along a 10 km-long transect (0 m, 1 km, 2 km, 5 km, 10 km from the TAG active vent) in the SSW direction from the vent. The Rosette was equipped with 16 Niskin 10-L bottles. Seawater samples for helium analyses were collected at three depths at each station and directly transferred from the Niskin bottles into crimped copper tubes following the procedure given by the Isotope Geochemistry Facility (Woods Hole Oceanographic Institution, https://www2.whoi.edu/site/igffacility/seawater-helium-isotopes-and-noble-gases/). Isotopic ^{3}He and ^{4}He analyses by mass spectrometer were performed in the same facility.

3 Topographic and Tidal Controls on the Dynamics

3.1 Overview

We first examine the power spectral densities (PSDs) of horizontal currents at TAG for the different simulations and the observations (Figure 2). PSDs reveal that TAG-REF produces realistic semi-diurnal internal tides compared to in situ observations. The semi-diurnal peak actually dominates across all frequencies up to monthly timescales. The near-inertial peak is also well represented, but there is an overall lack of energy across the whole internal wave band. This points towards the lack of representation of processes that likely occur at scales smaller than the ones represented in the simulation, and which would allow a more efficient direct energy cascade (e.g., Barkan et al., 2021).

At subinertial scales, TAG-REF slightly lacks energy in the 1-4-day range, where submesoscale processes occur. On the contrary, it produces energy levels that are above those observed for time scales of 5-30 days, i.e., the mesoscales. Again, this could be due to the processes involved in the direct energy cascade being only partially represented (Barkan et al., 2021). Within this time range, TAG-REF and TAG-NT have similar energy levels, an order of magnitude larger than the energy level in TAG-SB. This suggests that the topographic small scales strongly energize submesoscale dynamics.

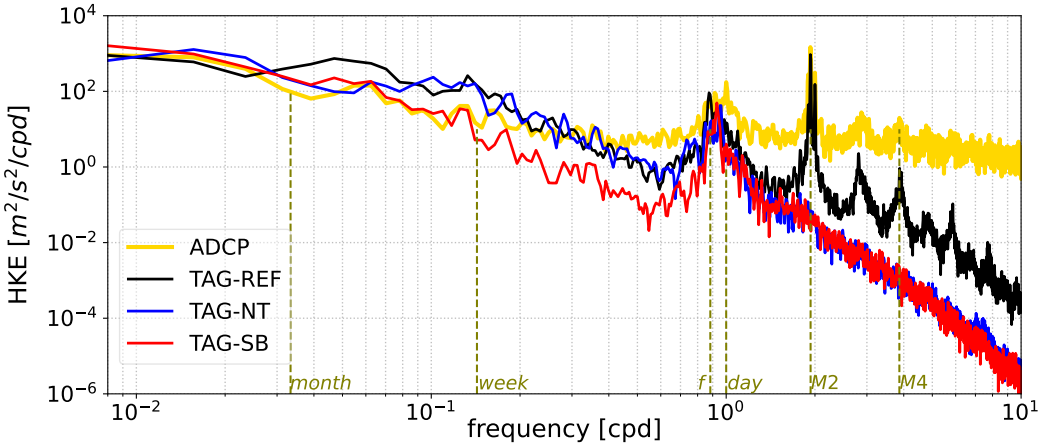

Figure 2. Power Spectral Density of horizontal currents (units of Horizontal Kinetic Energy (HKE) density) for ADCP currents (gold) and modeled currents in the simulations TAG-REF (black), TAG-NT (blue) and TAG-SB (red). The point in the simulations is located has the same height above the seafloor as for the ADCP data.

In the internal wave band (frequencies larger than f), TAG-NT and TAG-SB show very similar levels of energy, an order of magnitude smaller than in TAG-REF (Figure 2). This emphasizes the role of tidal forcing to energize the whole internal wave band.

In conclusion, both the tidal forcing and the topographic small scales are essential ingredients to feed both the internal wave field and the range of submesoscale variability. Next, we will examine specifically the imprint of these forcings on the dynamics.

3.2 Vorticity Production on Topographic Slopes

An animation of the potential vorticity field shows submesoscale structures in the currents generated on the ridge slopes in TAG-REF and TAG-NT (Supporting Information Movies S1 and S2). Here, potential vorticity (PV) is defined as $\mathbf{q} = \omega_a \cdot \nabla b$, the dot product of absolute vorticity $\omega_a = f\mathbf{z} + \nabla \times \mathbf{u}$ and the buoyancy gradient, with $b = -g\frac{\rho}{\rho_o}$, where f is the Coriolis parameter, $\mathbf{z}$ the unit vertical vector, ρ the in situ density, ρ_o the mean reference density, and $\mathbf{g}$ the gravitational acceleration (Gula et al., 2016). PV is a useful quantity to monitor as it is conserved in the absence of friction or diabatic fluxes, hence it has sources on the ocean's boundaries and can track open ocean coherent structures and water masses. It can also be used to diagnose submesoscale instabilities (Gula et al., 2016).

Submesoscale coherent vortices (SCVs) are routinely generated on the ridge and spread in the basin – an example is shown in Figures 3a-e through a sequence of PV formation on a topographic slope, detachment, and rolling up into an SCV. Sustained friction of low-frequency (not tidal) currents on slopes generates horizontal velocity shear and relative vorticity. This translates into extrema in PV, either negative or positive, depending on the direction of the low-frequency current compared to the topographic slope.

In Figures 3a-c, friction generates negative relative vorticity with a larger amplitude than the local Coriolis frequency, which means that the absolute vorticity is negative, and PV is negative too. This triggers an ageostrophic centrifugal instability and the subsequent formation of an anticyclonic eddy (Gula et al., 2016). The formation of cyclonic eddies through shear instability is also at play in the model. The SCVs generated on the topographic slopes of the ridge can be tracked for several months wandering around above the

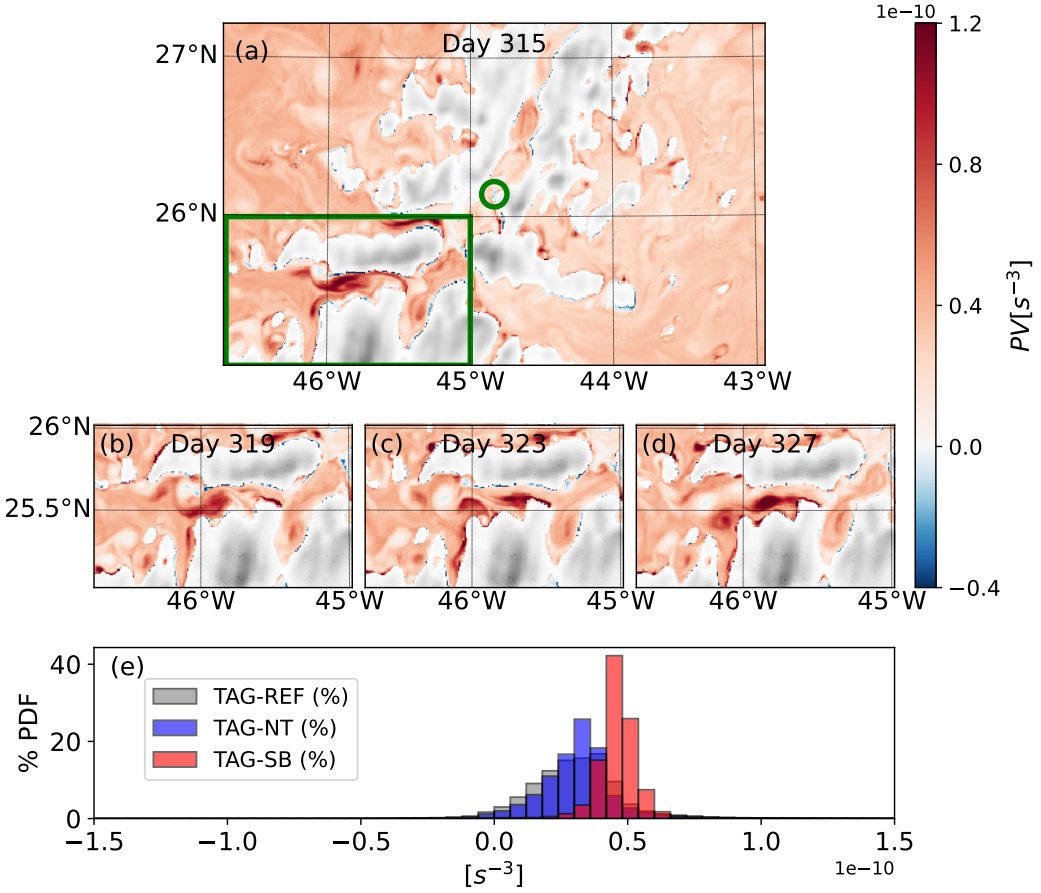

Figure 3. (a) to (d) show snapshots of PV in TAG-REF from day 315 to 327 (starting 1^{st} Jan. 2009, start of the simulation) at a depth of 3250 m. Gray shading shows bathymetry above 3250 m. The green circle shows TAG. In (a), the green rectangle shows the boundaries of maps shown in (b)-(d), which highlight a location of negative PV stripe formation that gives birth to an SCV in the following snapshots. (e) presents the probability density function of PV for TAG-REF, TAG-NT and TAG-SB, computed over the entire domain and over the 9-month integration period.

adjacent abyssal plain. As they carry material from the seafloor, we anticipate that they might be actively participating in the spreading of hydrothermal material. Although this phenomenology was uncovered at a much shallower hydrothermal vent site (Lucky Strike, ≈1700 m, Vic et al., 2018), to our knowledge, such regime of topographic turbulence deeper than 3000 m has not been reported.

There are much less SCVs in TAG-SB as compared to TAG-REF and TAG-NT (Supporting Information Movie S3). This is consistent with the energy drop within the submesoscale time range (time scales between a day and a week) in TAG-SB (Figure 2). Submesoscale topographic slopes have been shown to be essential to generate mesoscale and submesoscale variability (Rosso et al., 2015; Radko, 2020). Hence, removing those slopes in TAG-SB actually reduces submesoscale activity and in particular the generation of SCVs.

Figure 3f shows the distribution of PV for the three simulations at the same height above TAG for the final snapshot of the simulation. TAG-REF and TAG-NT exhibit similar distributions, although TAG-REF has a slightly larger proportion of negative PV. This

highlights that tidal currents can bolster submesoscale instabilities on slopes. This effect has been uncovered at the ocean surface in the wake of an island (see schematic in Figure 6 in MacKinnon et al., 2019). In contrast, TAG-SB is dominated by positive PV, whose distribution features much reduced tails compared to TAG-REF and TAG-NT, consistent with reduced extrema in relative vorticity produced by friction.

3.3 Vertical Diffusivity

Several physical processes lead to enhanced energy dissipation and mixing across isopycnals, termed diapycnal mixing, above the seafloor and in the adjacent hundreds of meters. Above a ridge such as the MAR, we expect internal tides to drive most of mixing (Vic et al., 2019), although submesoscale instabilities at the seafloor can also lead to mixing (Gula et al., 2022). The model simulations used here are able to partially resolve the direct energy cascade leading to tidal energy dissipation, and the submesoscale instabilities associated to mixing (PV<0, Section 3.2). The eventual mixing is parameterized through the KPP scheme, mostly relying on a critical Richardson number in the interior (not in boundary layers). If energy cascades down to sufficiently small scales to generate enough vertical velocity shear, Richardson-based mixing is activated in KPP, which results in increasing the vertical diffusivity coefficient.

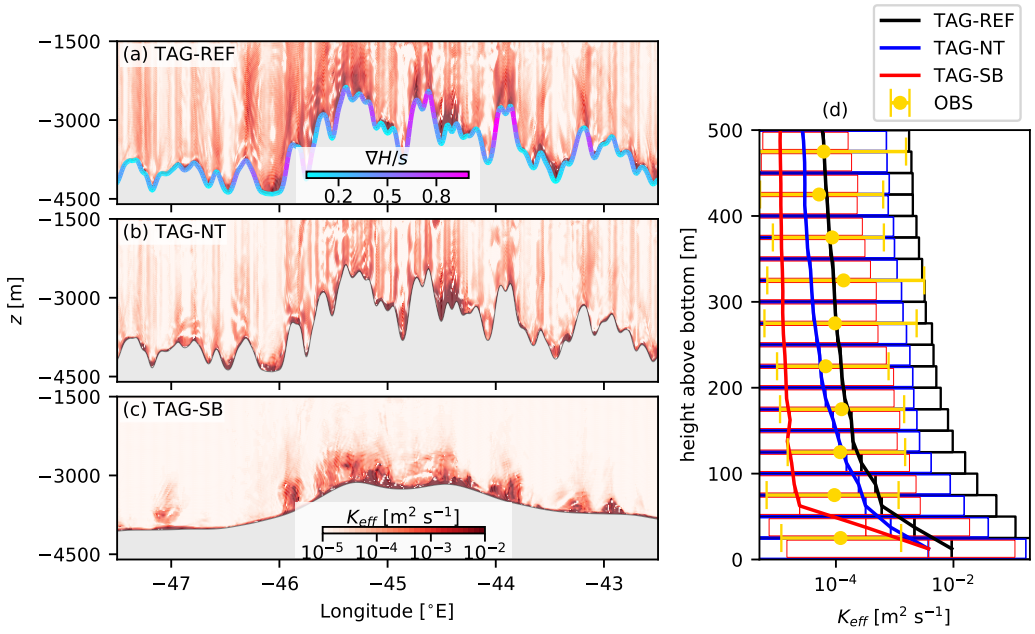

Figure 4. Vertical zonal section of effective mixing diffusivity K_{eff} in (a) TAG-REF, (b) TAG-NT and (c) TAG-SB averaged between days 5 and 10 days after the spinup stage. In (a), the slope criticality parameter $\nabla H/s$ is shown at the seafloor. (d) shows some statistics of K_{eff} as a function of height above bottom. For each 25-m bin, the 10^{th}, 50^{th} and 90^{th} percentiles of K_{eff} are shown for TAG-REF (black), TAG-NT (blue) and TAG-SB (red). The same quantities are shown in gold for the observationally-derived diffusivity (see Section 2.2).

In addition to the parameterized mixing, there is some numerical mixing linked to advection schemes (e.g., Marchesiello et al., 2009). A method to diagnose the total diapycnal mixing, i.e., parameterized plus numerical, was recently implemented in CROCO (Schifano et al., 2025). The method diagnoses an "effective diffusivity" K_{eff}, which is in general close

to the parameterized diffusivity in the bottom boundary layer, but can be larger in the open ocean, especially above steep slopes where numerical errors can be large. Figure 4 shows vertical sections of K_{eff} in TAG-REF, TAG-NT, and TAG-SB, and the distribution of K_{eff} as a function of height above bottom. Note that K_{eff} shown here was diagnosed online using the WENO5 advection schemes to reflect the numerical mixing experienced by the passive tracers. The actual diapycnal mixing (for density) in the simulation is smaller due to the use of the RSUP5 advection scheme for active tracers (see Section 2.1.1), in which the diffusive component is rotated along isopycnal surfaces. No such rotation is applied in WENO5, so the effective mixing is larger. However, WENO5 is still preferred for passive tracers because it reduces spurious oscillations and prevents negative tracer concentrations (Schifano et al., 2025). Figure 4 can be compared to Figure S2 in Supporting Information, which shows the parameterized diffusivity K_{KPP} for the three simulations along the same section and its vertical profiles too. Although K_{eff} and K_{KPP} show similar patterns and amplitudes within the bottom boundary layer, effective mixing largely exceeds parameterized mixing outside of the bottom boundary layer, for the three simulations. Nonetheless, although numerical mixing exceeds parameterized (physical) mixing in the interior, we argue that (i) it is influenced by physical processes and (ii) it bolsters the insufficient parameterized mixing to bring the effective mixing close to observations.

To support (i), we compare K_{eff} for TAG-REF and TAG-NT (Figures 4a,b,d). In TAG-REF, K_{eff} is enhanced over the ridge as compared to the adjacent abyssal plains, with local maxima near the seafloor reaching 10^{-2} m^2 s^{-1} and a vertical decay scale of 100-1000 m, before reaching 10^{-5} m^2 s^{-1}. Profiles show similar patterns in TAG-NT, although with a reduced amplitude. We interpret this difference as the contribution of internal tides. Above the MAR, the steep topographic slopes are expected to play a major role in the internal tide lifecycle: they generate energetic internal tides in the form of narrow beams (Vic & Ferron, 2023), and scatter internal tide energy to smaller scales (Lahaye et al., 2020), which promotes their local dissipation. Furthermore, internal wave breaking is enhanced in the vicinity of critical topographic slopes. The criticality parameter $\nabla H/s$, where ∇H is the topographic slope and s is the internal wave beam slope, $s = \left[(\omega^2 - f^2)/(N^2 - \omega^2)\right]^{1/2}$, where ω is the wave frequency (semidiurnal tidal frequency here) and N is the near-bottom buoyancy frequency. If $\nabla H/s$ approaches unity – in practice, the range 0.8-1.5 is often considered (e.g., Legg, 2014) –, the topographic slope is termed critical, and promotes wave breaking and mixing (Musgrave et al., 2022). The criticality parameter is shown in Figure 4a. $\nabla H/s$ hardly ever gets larger than unity but is often greater than 0.8, hence reaches near-critical values. Above near-critical slopes, K_{eff} is enhanced as compared to less steep slopes – this is also the case for K_{KPP} (Figure S2). This confirms that physical processes tied to internal tide energy dissipation lead to mixing in TAG-REF. In comparison, TAG-NT, in which internal tides are absent by construction, does not feature such enhanced mixing (Figure 4b and Figure 4d for a comparison of vertical profiles with TAG-REF). Furthermore, the propagation of internal tides is associated with displacements of isopycnal surfaces and amplifications of density gradients. The angle between isopycnals – along which advection should be performed, ideally – and σ-levels – along which advection is actually performed using WENO5 –, increases. As a consequence, spurious mixing through density surfaces increases. This joint physical-numerical process is absent from TAG-NT, which qualitatively explains the difference in K_{eff}.

To support (ii), we compared the effective diffusivity to in situ estimates of diffusivity from microstructure observations (Section 2.2 and Figure 4d). The numerical mixing seemingly brings the modeled effective mixing close to observations upward of ≈100 m above the bottom (Figure 4d); so, it might be considered as a placeholder to fill in for missing parameterized mixing at the current model resolution. In the bottommost 100 m, the model seems to generate too much mixing compared to observations. However, the observations used here are sparse in the lowest 100 m and only partially capture boundary processes (Polzin et al., 1997). Also, K_{eff} might be overestimated where stratification is very weak

due to methodological limitations (Schifano et al., 2025). These two biases could explain the divergence between the simulations and observations while approaching the seafloor.

TAG-SB displays much reduced levels of mixing, both within the boundary layer and in the ocean interior (Figure 4c). By construction, the difference with TAG-NT is solely explained by the smoother topographic slopes. Near the seafloor and in the adjacent hundreds of meters, there is a physical interpretation for this difference, linked to the lack of submesoscale instabilities associated with large slopes. Also, lee waves, generated by the interaction of balanced flows with the seafloor, can also dissipate their energy in the vicinity of the bottom. They are particularly bolstered by small-scale seafloor (Nikurashin et al., 2013). Their absence in TAG-SB could add up to the reduced submesoscale instabilities to explain the difference with TAG-NT (Figure 4d).

4 Spreading of Eulerian Tracers and Lagrangian Particles

In this section, we examine how tides and topography impact the dispersal of a hydrothermal tracer, and how the newly proposed Eulerian approach (considering the model resolution and application of the method to the deep ocean) differs from the more widely-used Lagrangian approach. We start with a brief description of the reference dispersal scenario based on TAG-REF (Section 4.1). Then, we study how tides and topography impact the dispersal (Section 4.2) and how the Eulerian and Lagrangian approaches differ (Section 4.3).

4.1 Reference scenario

The dispersal of TAG hydrothermal material was previously studied numerically through a Lagrangian approach that used the 3-dimensional velocity field of an Atlantic simulation with a grid spacing of 3 km, 100 vertical levels, and which shares similarities in the forcing with TAG-REF (Tagliabue et al., 2022). We thus expected the main dispersal pathways to be roughly similar, which happened to be the case. This section hence briefly describes the dispersal stages and pathways.

Figure 5 shows the dispersal patterns after different time scales from 10 days to 180 days. The early stages of the dispersal (10-30 days) are dominated by the northward and westward pathways (Figures 5a and 5b). The northward pathway is in the up-valley direction, which is consistent with the buoyancy-driven mean current over the northern MAR (Lahaye et al., 2019). The flow is constrained by the valley walls and the pathways to escape the valley are thus through transverse fracture zones such as the one extending west of the ridge at around 26°N.

At longer scales (60-90 days), the original pathways are still clearly visible and the tracer is also additionally stirred southward within the valley, opening another dispersal pathway, although containing less tracer than the northward and westward pathways (Figures 5c and 5d). Note that within the valley and fracture zones, the tracer is strongly mixed vertically (not shown). After 60-90 days, mixing has operated for long enough to spread the tracer vertically to shallower depths, allowing it to pass over some topographic structures – for example, over the hill ≈50 km west of TAG (Figure 5d).

After 90 days, the tracer has massively escaped from the valley westward (Figures 5d-f). The imprint of eddies on tracer concentration is visible. Some high concentration is found within eddies that are formed over the MAR and travel westward. The asymmetry between the preferred westward pathway and the almost inexistent eastward pathway can be explained by the westward drift of freely-evolving oceanic eddies (Killworth, 1983).

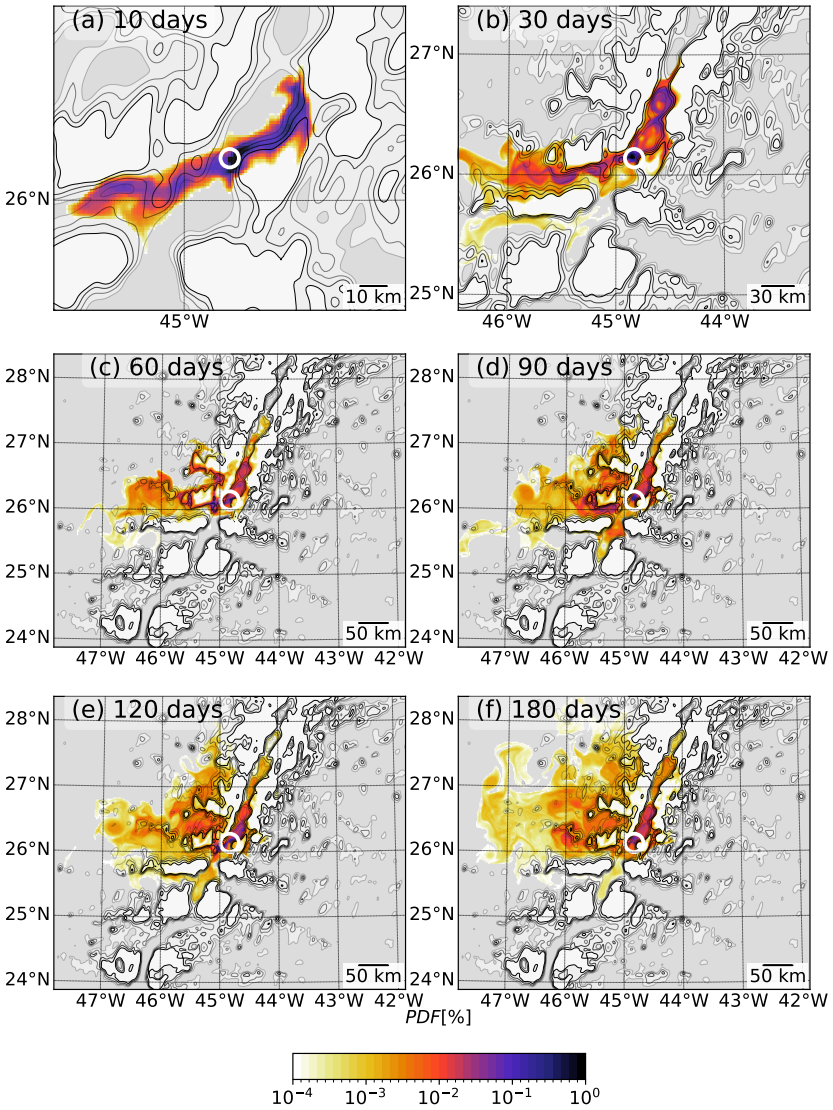

Figure 5. Tracer distribution after (a) 10, (b) 30, (c) 60, (d) 90, (e) 120 and (f) 180 days in TAG-REF. The white circle shows TAG. The black contours represent isobaths 3000, 3200, 3400 and 3600 m. Bathymetry is shaded in dark gray below 3600 m and in light gray between 3000 and 3600 m.

4.2 How tides and small-scale topography impact the dispersal

Figures 6a-c compare the horizontal distribution of tracer at the end of the simulation, 260 days after their initial release. TAG-REF and TAG-NT display similar dispersal patterns, with most of the tracer in the valley and west of the ridge, consistently with the reference dispersal scenario (Section 4.1). The fine scale patterns of the distributions, shaped for example by eddies or filaments, are not strictly the same because of the intrinsic nonlinearities in the model that lead to divergence in the location and timing of turbulent events at all scales.

The most striking difference in the horizontal distributions of tracer is between TAG-REF/TAG-NT and TAG-SB (Figures 6a and 6b vs 6c). In the latter, the tracer seems

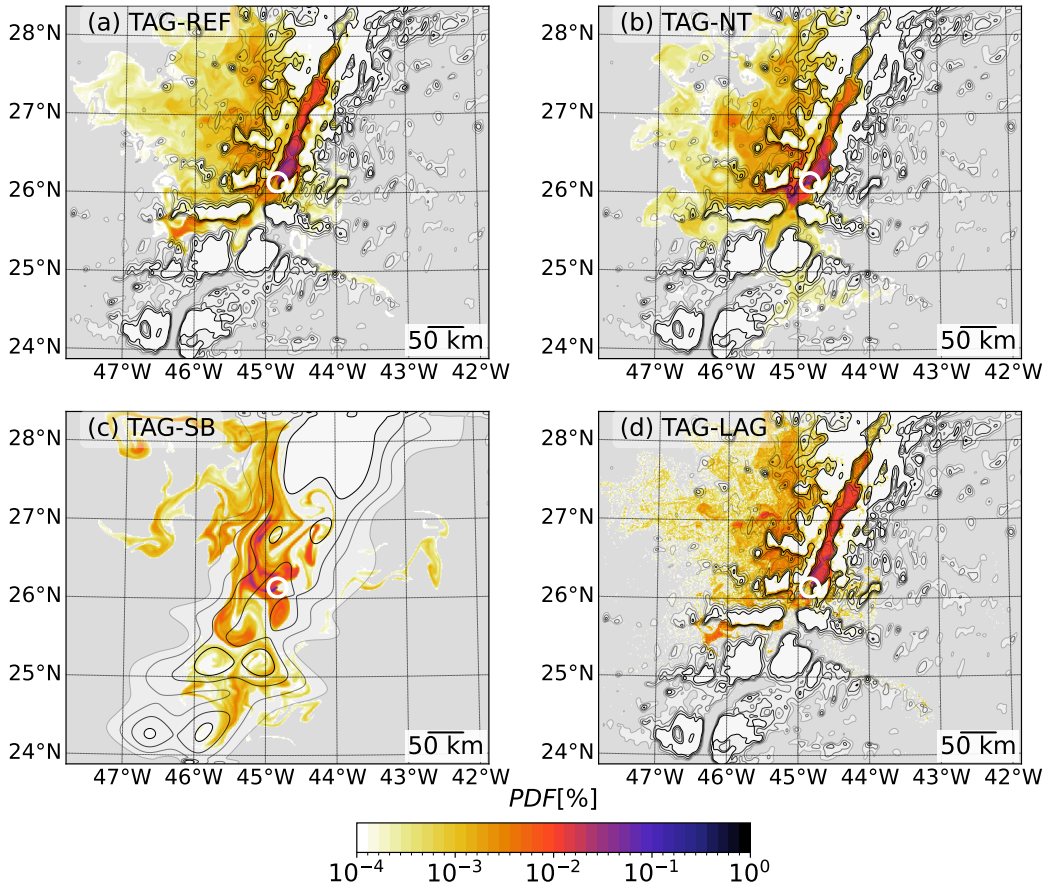

Figure 6. Probability density function of tracer after 260 days for (a) TAG-REF, (b) TAG-NT, (c) TAG-SB and (d) TAG-LAG. For the latter, We used 5×5-km^2 bins to count particles. Bathymetry contours are as in Figure 5.

to be mostly confined above the ridge and hardly gets west of 46°W as compared to TAG-REF/TAG-NT. This is at first sight surprising since there is no topographic barrier in TAG-SB that would impede an off-ridge transport. We argue that the absence of topographic submesoscale instabilities, hence SCVs, in TAG-SB at the tracer depth explains the very limited westward transport. Instead, the tracer is stirred by the low-frequence, mesoscale, currents. The comparison of these experiments highlights the important role played by SCVs in the off-ridge transport of hydrothermal material.

Figures 7a-c present vertical sections of tracer in TAG-REF, TAG-NT and TAG-SB at the end of the simulation. Again, TAG-REF and TAG-NT show similar patterns with most of the tracer sitting on $\sigma_3 \approx 41.48 - 41.56$. The vertical distribution of the tracer over the whole domain confirms the similarity between TAG-REF and TAG-NT (Figure 8a). On long time scales, the net mixing effect of tides, which mostly occurs over the ridge, does not seem to play a role in the vertical spreading of the tracer (see also Figure 8b).

In TAG-SB, the tracer is confined to a much narrower density layer ($\sigma_3 \approx 41.48 - 41.52$, Figure 7c). Note that the tracer is released following a distribution in height above the bottom at TAG (Section 2.1.2), which leads to different depth distributions in TAG-REF/TAG-NT vs TAG-SB as the seafloor depth at TAG is not the same for the two bathymetries (Figures 7a vs 7c). In consequence, the exact comparison of the depth or density layers that

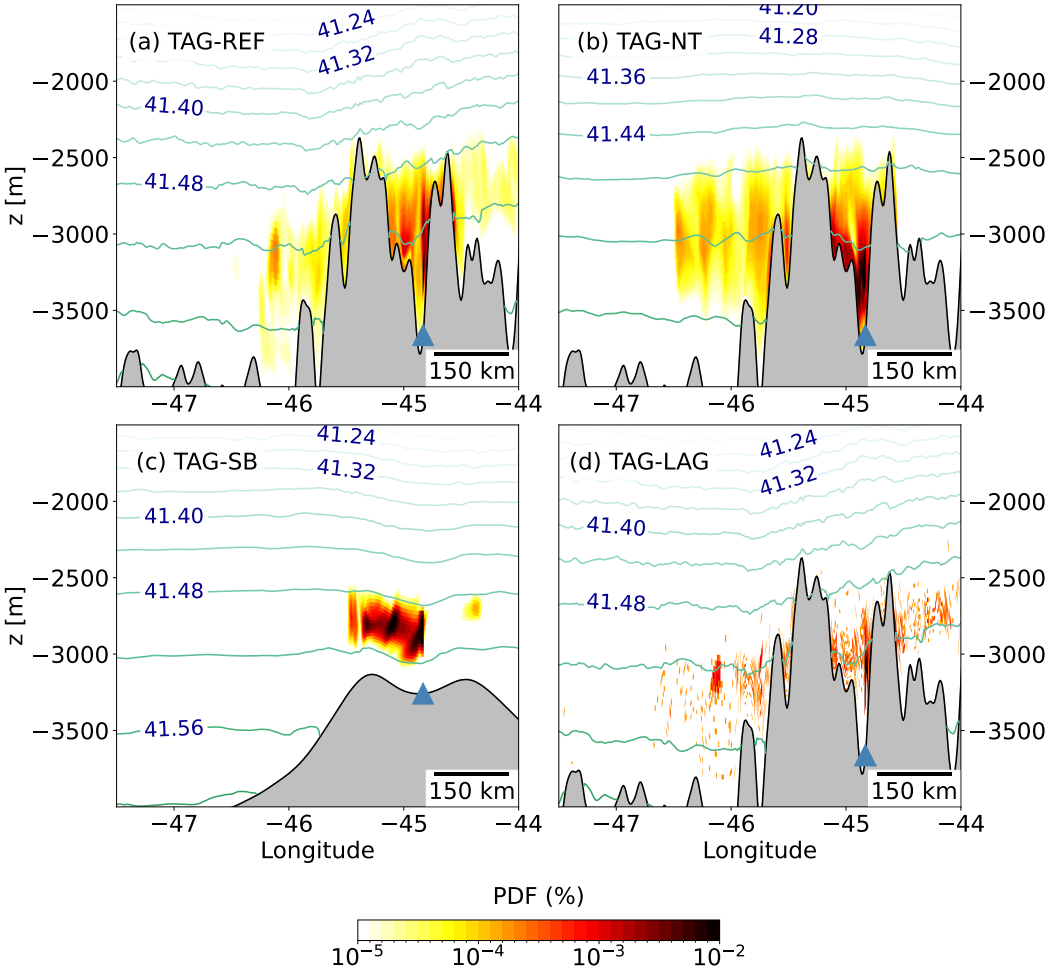

Figure 7. Zonal and vertical section of the tracer on day 260 in (a) TAG-REF, (b) TAG-NT, (c) TAG-SB, and (d) TAG-LAG. TAG is shown by the blue marker. The green lines represent density referenced at 3000 m (σ_3) with a spacing of 0.04 kg m^{-3}.

host the tracer is not meaningful. However, the change of the tracer distribution in depth or density is meaningful. Because of reduced mixing in TAG-SB, the tracer does not cross as many density layers as in TAG-REF and TAG-NT (Figure 8a). Its vertical distribution has smaller tails in TAG-SB as compared to TAG-REG and TAG-NT (Figure 8b). These distributions emphasize the important role that mixing has on the vertical distribution of the tracer. In the model, mixing is influenced primarily by topographic slopes and to a lesser extent by tides (Figure 4). Consequently, smoothing drastically the bathymetry has a larger effect on the vertical spreading of the tracer than switching off the tides (Figure 8b).

Note that after 260 days, the tracer has undergone diapycnal upwelling and downwelling in nearly equal proportions for all simulations (see mean in Figure 8a). So, there does not seem to be a net effect of advection and mixing in driving a significant upwelling or downwelling for a tracer released far above the bottom boundary layer.

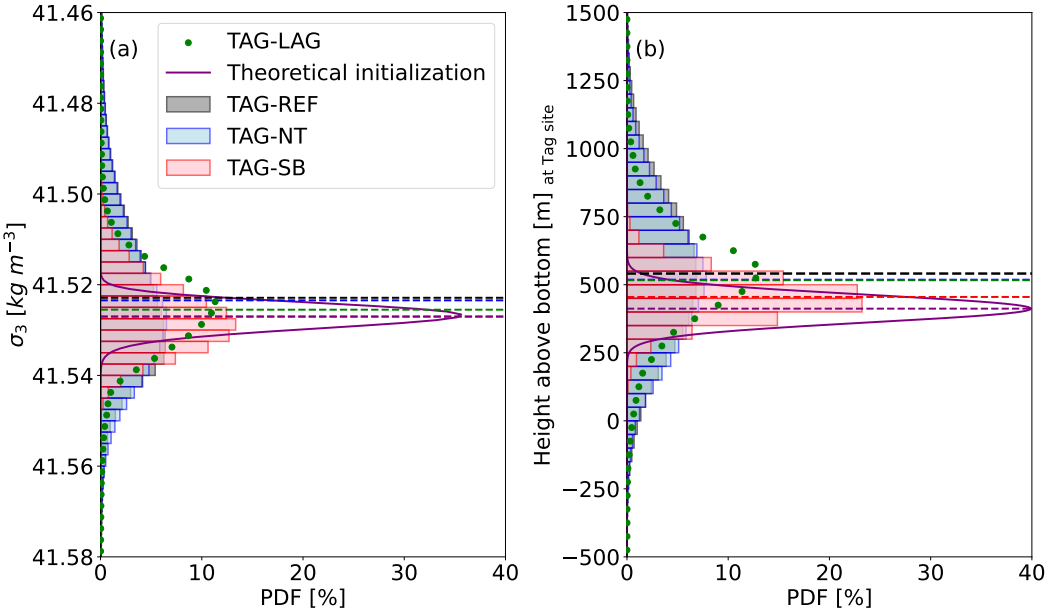

Figure 8. Distribution of the tracer after 260 days as a function of (a) potential density referenced at 3000 m and (b) height above the bottom referenced at TAG, in (black) TAG-REF, (blue) TAG-NT and (red) TAG-SB. The distribution for TAG-LAG is shown with green dots. The dashed lines represent the mean of each distribution (TAG-REF: $\sigma_3 = 41.523$, hab=540 m, TAG-NT: $\sigma_3 = 41.523$, hab=518 m, TAG-SB: $\sigma_3 = 41.527$, hab=455 m, TAG-LAG: $\sigma_3 = 41.525$, hab=516 m). The analytical distribution of tracer at the source is shown in purple ($\sigma_3 = 41.527$, hab=412 m).

4.3 Eulerian vs Lagrangian dispersal

The horizontal distributions of the Eulerian tracer in TAG-REF and of the Lagrangian particles in TAG-LAG look very similar (Figures 6a and 6d). Both the large-scale spreading patterns and the smaller-scale eddying structures trapping material are very comparable. There seems to be small differences on the valley walls where more tracer has accumulated in TAG-REF compared to particles in TAG-LAG. This is consistent with the distribution of tracer vs particles through the vertical section, where the envelope of the tracer reaches shallower depths above steep and small-scale topographic structures (Figures 7a vs 7d). This means that mixing in TAG-REF has helped the tracer to spread to shallower depths – recall that mixing is not explicitly included in TAG-LAG. This is confirmed by the distributions in density space and in the vertical (Figure 8). The shapes of the distributions are roughly comparable apart from their tails, which are much thicker in TAG-REF as compared to TAG-LAG. The difference could be seen as the net effect of including mixing (parametrized and numerical) in the Eulerian framework as compared to the Lagrangian framework.

To further investigate the role of mixing in the diapycnal spreading of material, we had a closer look at the distributions of tracer and particles in σ_3 space at different spatial points (not shown). It appears that the distributions in TAG-REF most often have larger tails for lighter σ_3 classes (this is also the case in Figure 8a), which translates into a negative skewness. This information is synthesized in Figure 9a, which shows the skewness of the distribution of tracer in TAG-REF in σ_3 space for each 5×5-km^2 bin. On the contrary, in TAG-LAG, the skewness of the same distribution (but for particles instead of tracer) is mostly negative within the valley and positive outside (Figure 9b). Our interpretation is

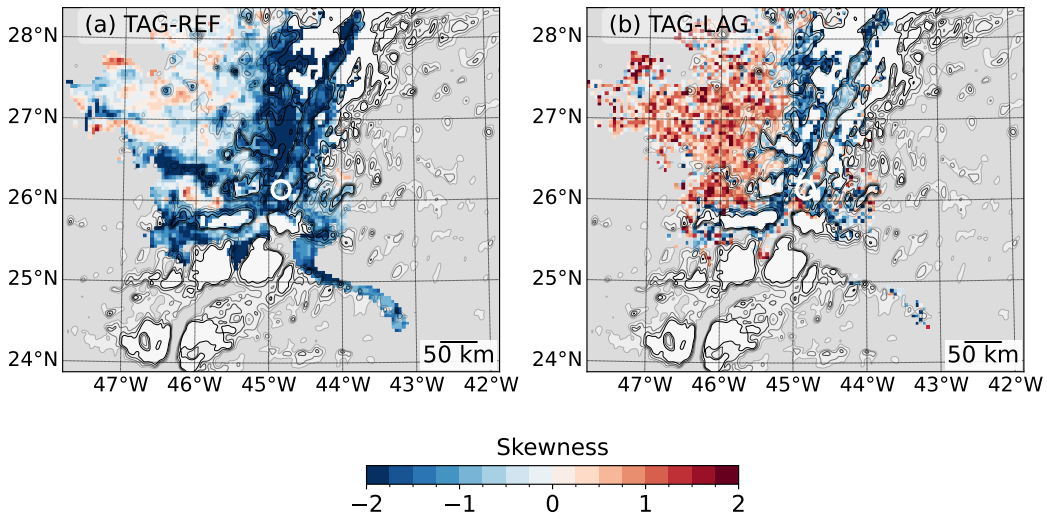

Figure 9. Maps showing in each 5×5-km^2 bin the skewness of the distribution in σ_3 space of (a) tracer in TAG-REF and (b) particles in TAG-LAG. Bathymetry contours are as in Figure 5.

twofold. First, mixing drives an asymmetry in the diapycnal spreading, with a tendency to upwell a small portion of the tracer to very light density classes. Second, in the absence of explicit mixing (TAG-LAG), advection has a similar effect in the vicinity of small-scale topographic structures with large slopes above the MAR: it tends to rise a small portion of particles to very light density classes. Off the MAR, on the contrary, advection tends to move particles to heavier density classes.

In conclusion, the comparison of Eulerian and Lagrangian experiments shows that the horizontal dispersal patterns are very similar, both at the large-scale and within eddying structures. The Lagrangian experiment shows reduced vertical spreading, due to the absence of explicit vertical mixing, but this does not change qualitatively the spreading patterns after several months. This is consistent with the numerical experiments carried out at the surface in a coarser-resolution model (Wagner et al., 2019).

5 Summary and Discussion

We designed and ran high-resolution numerical experiments to disentangle the role of tides and small-scale bathymetry in the deep-ocean dynamics above the MAR and their effects on the dispersal of hydrothermal material from TAG. A tracer is continuously injected in the simulations following an analytical distribution constrained by in situ observations of helium, considered as a biochemically inert hydrothermal tracer, whose fate is solely driven by physical processes. Our tracer experiments would be representative of the fate of such a tracer, without considering biogeochemical processes that would alter its state and concentration. We also performed Eulerian and Lagrangian experiments to test how those two frameworks impact the dispersal. Results can be summarized as follows.

- Kilometer-scale seafloor topography is essential to catalyze submesoscale instabilities and generate submesoscale eddies. The interaction of currents with small-scale topography actually raises kinetic energy in the submesoscale time range by an order of magnitude as compared to a simulation with a smooth topography.
- These submesoscale eddies are instrumental in the horizontal spreading of hydrothermal material off the ridge, above the adjacent abyssal plain. In the smooth-bathymetry

simulation, the tracer is almost confined to the ridge, as if it were only advected by low-frequency laminar currents. The net effect of topographic submesoscale eddies is thus to augment the horizontal spreading. They actually offset the effect of adding topographic barriers through the inclusion of small-scale bathymetry.

- Tides increase vertical diffusivity above the ridge, especially above near-critical slopes where internal tides dissipate their energy. Including tides to the simulation increases the model effective diffusivity up to observed diffusivity, hence it increases the realism of the simulation. However, tides do not have a notable effect on the vertical spreading of hydrothermal tracers. On long time scales, their impact on the horizontal spreading pathways is negligible.
- Eulerian and Lagrangian experiments lead to very similar horizontal spreading patterns, both on the large-scale and at the scale of eddying structures. Even if the vertical spreading is increased for the Eulerian tracer due to diffusion effects absent in the Lagrangian experiment, this does not change qualitatively the horizontal spreading patterns.

Perhaps the most spectacular result of this study is the impact of small-scale seafloor topography in the generation of submesoscale eddies, and their subsequent effect on the horizontal spreading, which is massive and was unanticipated at this depth. Global simulations do not resolve such small scales and spreading patterns of hydrothermal material are not realistic (e.g., Figure 3a in Tagliabue et al., 2022). Biased spreading pathways change the oceanic journey of deep-ocean material and likely impact the lifecycle of some hydrothermal compounds of climate relevance, such as iron. One might wonder how to deal with these biases in global budgets. It raises the question of how to improve the spreading pathways in global models at an acceptable computational cost, without resolving explicitly the topographic submesoscale turbulence.

Our study highlights the strength of Lagrangian models in capturing horizontal spreading pathways at the submesoscales. Their inherent limitation in the representation of vertical diffusion processes does not impact qualitatively the horizontal spreading, similarly to the results of a previous study that focused on the surface dispersal (Wagner et al., 2019). Given the relatively low computational cost of Lagrangian simulations, they prove to be a powerful tool to simulate the dispersal of passive material in the deep ocean. Furthermore, their misrepresentation of vertical spreading can be mitigated by incorporating stochastic diffusion (e.g., Onink et al., 2022).

Finally, this study establishes a robust modeling framework to further investigate the fate of hydrothermal iron, which is still not well constrained, despite having a strong significance in climate-scale biogeochemical budgets (Bühring et al., 2025). We now have a clear view of the physical ingredients operating at scales greater than ≈10 km that need to be incorporated to the simulations to get a realistic plume representation.

Conflict of Interest Statement

The authors have no conflicts of interest to disclose.

Open Research Section

We used the CROCO-PISCES ocean model from Auclair et al. (2025). Further information is provided at https://www.croco-ocean.org and https://www.pisces-community.org. The World Ocean Atlas 2023 dataset is from Garcia et al. (2024). The Lagrangian software Pyticles is from Gula and Collin (2021).

Acknowledgments
This work benefited from French State aid managed by the National Research Agency

under France 2030 LIFEDEEPER (ANR-22-POCE-0007), and DEEPER (ANR-19-CE01-0002-01). We thank Mathieu Le Corre, Gildas Cambon, Pierre-Amaël Auger, Christian Ethé and Renaud Person for their help in setting up the model configuration.

References

Ardyna, M., Lacour, L., Sergi, S., d'Ovidio, F., Sallée, J.-B., Rembauville, M., ... others (2019). Hydrothermal vents trigger massive phytoplankton blooms in the Southern Ocean. *Nature communications*, *10*(1), 2451. doi: 10.1038/s41467-019-09973-6

Auclair, F., Benshila, R., Bordois, L., Boutet, M., Brémond, M., Caillaud, M., ... Valat, S. (2025, March). *Coastal and Regional Ocean COmmunity model [software].* Zenodo. Retrieved from `https://doi.org/10.5281/zenodo.15064113` doi: 10.5281/zenodo.15064113

Aumont, O., Éthé, C., Tagliabue, A., Bopp, L., & Gehlen, M. (2015). PISCES-v2: an ocean biogeochemical model for carbon and ecosystem studies. *Geosci. Model Dev.*, *8*(2). doi: 10.5194/gmd-8-2465-2015

Baker, E. T., & German, C. R. (2004). On the global distribution of hydrothermal vent fields. *Mid-Ocean Ridges: Hydrothermal Interactions Between the Lithosphere and Oceans, Geophys. Monogr. Ser*, *148*, 245–266.

Barkan, R., Srinivasan, K., Yang, L., McWilliams, J. C., Gula, J., & Vic, C. (2021). Oceanic mesoscale eddy depletion catalyzed by internal waves. *Geophysical Research Letters*, *48*(18), e2021GL094376. doi: 10.1029/2021GL094376

Becker, J., Sandwell, D., Smith, W., Braud, J., Binder, B., Depner, J., ... others (2009). Global bathymetry and elevation data at 30 arc seconds resolution: SRTM30_PLUS. *Marine Geodesy*, *32*(4), 355–371. doi: 10.1080/01490410903297766

Breusing, C., Biastoch, A., Drews, A., Metaxas, A., Jollivet, D., Vrijenhoek, R. C., ... others (2016). Biophysical and population genetic models predict the presence of "phantom" stepping stones connecting Mid-Atlantic Ridge vent ecosystems. *Current Biology*, *26*(17), 2257–2267. doi: 10.1016/j.cub.2016.06.062

Bühring, S. I., Böhnke-Brandt, S., Diehl, A., Gledhill, M., Haffert, L., Kleint, C., ... others (2025). Iron's irony: speciation, complexation & microbial processing of fe in hydrothermal plumes. *Communications Earth & Environment*, *6*(1), 821. doi: 10.1038/s43247-025-02839-4

Cambon, M.-A., & Pelleter, E. (2025). The LIFEDEEPER Project: LIving together in the Future: vulnErability of DEEP sea Ecosystems facing potential mineral Resources exploitation. In *OOS2025-One Ocean Science Congress. 3-6 June 2025, Nice, France.*

Clément, L., Thurnherr, A. M., & St. Laurent, L. C. (2017). Turbulent mixing in a deep fracture zone on the Mid-Atlantic Ridge. *J. Phys. Oceanogr.*, *47*(8), 1873–1896. doi: 10.1175/JPO-D-16-0264.1

Cuvelier, D., Legendre, P., Laës-Huon, A., Sarradin, P.-M., & Sarrazin, J. (2017). Biological and environmental rhythms in (dark) deep-sea hydrothermal ecosystems. *Biogeosciences*, *14*(12), 2955–2977.

Debreu, L., & Blayo, E. (2008). Two-way embedding algorithms: a review. *Ocean Dynamics*, *58*(5-6), 415–428. doi: 10.1007/s10236-008-0150-9

de Lavergne, C., Falahat, S., Madec, G., Roquet, F., Nycander, J., & Vic, C. (2019). Toward global maps of internal tide energy sinks. *Ocean Modelling*, *137*, 52–75. doi: 10.1016/j.ocemod.2019.03.010

Fitzsimmons, J. N., John, S. G., Marsay, C. M., Hoffman, C. L., Nicholas, S. L., Toner, B. M., ... Sherrell, R. M. (2017). Iron persistence in a distal hydrothermal plume supported by dissolved–particulate exchange. *Nature Geoscience*, *10*(3), 195–201. doi: 10.1038/NGEO2900

Fouquet, Y., Pelleter, W., & Cathalot, C. (2017). *HERMINE cruise, R/V Pourquoi Pas ?* doi: 10.17600/17000200

Frenger, I., Bianchi, D., Stührenberg, C., Oschlies, A., Dunne, J., Deutsch, C., ... Schütte, F. (2018). Biogeochemical role of subsurface coherent eddies in the ocean: Tracer

cannonballs, hypoxic storms, and microbial stewpots? *Global Biogeochemical Cycles*, *32*(2), 226–249. doi: 10.1002/2017GB005743

Früh-Green, G. L., Kelley, D. S., Lilley, M. D., Cannat, M., Chavagnac, V., & Baross, J. A. (2022). Diversity of magmatism, hydrothermal processes and microbial interactions at mid-ocean ridges. *Nature Reviews Earth & Environment*, *3*(12), 852–871. doi: 10.1038/s43017-022-00364-y

Fujioka, K., Kobayashi, K., Kato, K., Aoki, M., Mitsuzawa, K., Kinoshita, M., & Nishizawa, A. (1997). Tide-related variability of TAG hydrothermal activity observed by deep-sea monitoring system and OBSH. *Earth and Planetary Science Letters*, *153*(3-4), 239–250.

Furushima, Y., & Yamamoto, H. (2014). Periodic behavior of deep sea current in the Hatoma Knoll hydrothermal system. In *Subseafloor biosphere linked to hydrothermal systems: Taiga concept* (pp. 625–637). Springer.

Garcia, H. E., Bouchard, C., Cross, S. L., Paver, C. R., Reagan, J. R., Boyer, T. P., ... others (2024). World ocean atlas 2023, volume 4: Dissolved inorganic nutrients (phosphate, nitrate, and silicate) [dataset]. Retrieved from `https://www.ncei.noaa.gov/access/world-ocean-atlas-2023/`

Gaube, P., McGillicuddy Jr, D. J., Chelton, D. B., Behrenfeld, M. J., & Strutton, P. G. (2014). Regional variations in the influence of mesoscale eddies on near-surface chlorophyll. *Journal of Geophysical Research: Oceans*, *119*(12), 8195–8220.

González-Santana, D., Planquette, H., Cheize, M., Whitby, H., Gourain, A., Holmes, T., ... others (2020). Processes driving iron and manganese dispersal from the TAG hydrothermal plume (Mid-Atlantic Ridge): results from a GEOTRACES process study. *Frontiers in Marine Science*, *7*, 568. doi: 10.3389/fmars.2020.00568

Gregg, M., D'Asaro, E., Riley, J., & Kunze, E. (2018). Mixing efficiency in the ocean. *Annu. Rev. Mar. Sci.*, *10*, 443–473. doi: 10.1146/annurev-marine-121916-063643

Gula, J., & Collin, J. (2021). *Pyticles: a python/fortran hybrid parallelized code for 3d lagrangian particles advection using roms/croco model data [software].* Zenodo. Retrieved from `https://doi.org/10.5281/zenodo.4973786` doi: 10.5281/zenodo.4973786

Gula, J., Molemaker, M. J., & McWilliams, J. C. (2014). Submesoscale cold filaments in the Gulf Stream. *Journal of Physical Oceanography*, *44*(10), 2617–2643. doi: 10.1175/JPO-D-14-0029.1

Gula, J., Molemaker, M. J., & McWilliams, J. C. (2016). Topographic generation of submesoscale centrifugal instability and energy dissipation. *Nature Communications*, *7*. doi: 10.1038/ncomms12811

Gula, J., Taylor, J., Shcherbina, A., & Mahadevan, A. (2022). Submesoscale processes and mixing. In *Ocean mixing* (pp. 181–214). doi: 10.1016/B978-0-12-821512-8.00015-3

Gula, J., Theetten, S., Cambon, G., & Roullet, G. (2021, June). *Description of the GIGATL simulations.* Zenodo. Retrieved from `https://doi.org/10.5281/zenodo.4948523` doi: 10.5281/zenodo.4948523

Jean-Baptiste, P., Charlou, J., Stievenard, M., Donval, J., Bougault, H., & Mevel, C. (1991). Helium and methane measurements in hydrothermal fluids from the mid-Atlantic ridge: The Snake Pit site at 23 N. *Earth and Planetary Science Letters*, *106*(1-4), 17–28.

Jiang, G.-S., & Shu, C.-W. (1996). Efficient implementation of weighted eno schemes. *Journal of computational physics*, *126*(1), 202–228.

Killworth, P. D. (1983). On the motion of isolated lenses on a beta-plane. *Journal of Physical Oceanography*, *13*(3), 368–376.

Klein, P., & Lapeyre, G. (2009). The oceanic vertical pump induced by mesoscale and submesoscale turbulence. *Annu. Rev. Mar. Sci.*, *1*, 351–375. doi: 10.1146/annurev.marine.010908.163704

Lahaye, N., Gula, J., & Roullet, G. (2020). Internal tide cycle and topographic scattering over the North Mid-Atlantic Ridge. *Journal of Geophysical Research: Oceans*, *125*(12), e2020JC016376. doi: 10.1029/2020JC016376

Lahaye, N., Gula, J., Thurnherr, A. M., Reverdin, G., Bouruet-Aubertot, P., & Roullet, G. (2019). Deep currents in the rift valley of the North Mid-Atlantic Ridge. *Frontiers in Marine Science*, *6*, 597. doi: 10.3389/fmars.2019.00597

Large, W., McWilliams, J., & Doney, S. (1994). Oceanic vertical mixing: A review and a model with a nonlocal boundary layer parameterization. *Rev. Geophys.*, *32*(4), 363–403. doi: 10.1029/94RG01872

Legg, S. (2014). Scattering of low-mode internal waves at finite isolated topography. *Journal of Physical Oceanography*, *44*(1), 359–383. doi: 10.1175/JPO-D-12-0241.1

Lemaréchal, C., Roullet, G., & Gula, J. (2025). Hydrothermal plume near-field dynamics from LES and observations. *Journal of Geophysical Research: Oceans*, *130*(10), e2024JC022277. doi: 10.1029/2024JC022277

Lemarié, F., Debreu, L., Shchepetkin, A., & Mcwilliams, J. C. (2012). On the stability and accuracy of the harmonic and biharmonic isoneutral mixing operators in ocean models. *Ocean Modell.*, *52*, 9–35. doi: 10.1016/j.ocemod.2012.04.007

Lemarié, F., Kurian, J., Shchepetkin, A. F., Jeroen Molemaker, M., Colas, F., & McWilliams, J. C. (2012). Are there inescapable issues prohibiting the use of terrain-following coordinates in climate models? *Ocean Modelling*, *42*, 57–79. doi: 10.1016/j.ocemod.2011.11.007

Lévy, M., Couespel, D., Haëck, C., Keerthi, M. G., Mangolte, I., & Prend, C. J. (2024). The impact of fine-scale currents on biogeochemical cycles in a changing ocean. *Annual Review of Marine Science*, *16*(1), 191–215. doi: 10.1146/annurev-marine-020723-020531

Lévy, M., Franks, P. J., & Smith, K. S. (2018). The role of submesoscale currents in structuring marine ecosystems. *Nature Communications*, *9*(1), 4758. doi: 10.1038/s41467-018-07059-3

Lupton, J. E. (1998). Hydrothermal helium plumes in the pacific ocean. *Journal of Geophysical Research: Oceans*, *103*(C8), 15853–15868.

Lupton, J. E., Baker, E. T., Garfield, N., Massoth, G. J., Feely, R. A., Cowen, J. P., ... Rago, T. A. (1998). Tracking the evolution of a hydrothermal event plume with a RAFOS neutrally buoyant drifter. *Science*, *280*(5366), 1052–1055.

Lutz, R. A., & Kennish, M. J. (1993). Ecology of deep-sea hydrothermal vent communities: A review. *Reviews of geophysics*, *31*(3), 211–242.

MacKinnon, J. A., Alford, M. H., Voet, G., Zeiden, K., Johnston, T. S., Siegelman, M., ... Merrifield, M. (2019). Eddy wake generation from broadband currents near Palau. *J. Geophys. Res. Oceans*, *124*(7), 4891–4903. doi: 10.1029/2019JC014945

Marchesiello, P., Debreu, L., & Couvelard, X. (2009). Spurious diapycnal mixing in terrain-following coordinate models: The problem and a solution. *Ocean Modelling*, *26*(3), 156–169. doi: 10.1016/j.ocemod.2008.09.004

Martin, W., & Russell, M. J. (2007). On the origin of biochemistry at an alkaline hydrothermal vent. *Philosophical Transactions of the Royal Society B: Biological Sciences*, *362*(1486), 1887–1926. doi: 10.1098/rstb.2006.1881

Mashayek, A., Gula, J., Baker, L. E., Naveira Garabato, A. C., Cimoli, L., Riley, J. J., & de Lavergne, C. (2024). On the role of seamounts in upwelling deep-ocean waters through turbulent mixing. *Proceedings of the National Academy of Sciences*, *121*(27), e2322163121. doi: 10.1073/pnas.2322163121

Matabos, M., Cannat, M., Ballu, V., Barreyre, T., Blandin, J., Castillo, A., ... others (2025). The EMSO-Azores deep-sea observatory: 15 years of multidisciplinary studies of the lucky strike hydrothermal system, from sub-seafloor to the water column. *Journal of Sea Research*, 102625. doi: 10.1016/j.seares.2025.102625

McCoy, D., Bianchi, D., & Stewart, A. L. (2020). Global observations of submesoscale coherent vortices in the ocean. *Progress in Oceanography*, *189*, 102452. doi: 10.1016/j.pocean.2020.102452

Ménesguen, C., Ducousso, N., Vic, C., & Le Gentil, S. (2025). Exploring baroclinic instability of the computational kind (BICK) in numerical simulations of the ocean. *Journal of Advances in Modeling Earth Systems*, *17*(4). doi: 10.1029/2024MS004600

Musgrave, R., Pollmann, F., Kelly, S., & Nikurashin, M. (2022). The lifecycle of

topographically-generated internal waves. In *Ocean mixing* (pp. 117–144). Elsevier. doi: 10.1016/B978-0-12-821512-8.00013-X

Naveira Garabato, A. C., Spingys, C. P., Castro, B. F., Couto, N., Drake, H. F., Forryan, A., ... others (2025). Connecting mixing to upwelling along the ocean's sloping boundary. *Geophysical Research Letters*, *52*(22), e2025GL119186. doi: 10.1029/2025GL119186

Nikurashin, M., Vallis, G. K., & Adcroft, A. (2013). Routes to energy dissipation for geostrophic flows in the Southern Ocean. *Nature Geosci.*, *6*(1), 48. doi: 10.1038/NGEO1657

Nishioka, J., Obata, H., & Tsumune, D. (2013). Evidence of an extensive spread of hydrothermal dissolved iron in the indian ocean. *Earth and Planetary Science Letters*, *361*, 26–33. doi: 10.1016/j.epsl.2012.11.040

Onink, V., Van Sebille, E., & Laufkötter, C. (2022). Empirical Lagrangian parametrization for wind-driven mixing of buoyant particles at the ocean surface. *Geoscientific Model Development*, *15*(5), 1995–2012. doi: 10.5194/gmd-15-1995-2022

Osborn, T. (1980). Estimates of the local rate of vertical diffusion from dissipation measurements. *Journal of Physical Oceanography*, *10*(1), 83–89.

Pelleter, E.-L., Principaud, M., Alix, A.-S., Boissier, A., Cheron, S., Besson, F., ... others (2024). Diversity, spatial distribution and evolution of inactive and weakly active hydrothermal deposits in the TAG hydrothermal field. *Frontiers in Earth Science*, *12*, 1304993. doi: 10.3389/feart.2024.1304993

Polzin, K., Toole, J., Ledwell, J., & Schmitt, R. (1997). Spatial variability of turbulent mixing in the abyssal ocean. *Science*, *276*(5309), 93–96. doi: 10.1126/science.276.5309.93

Radko, T. (2020). Control of baroclinic instability by submesoscale topography. *Journal of Fluid Mechanics*, *882*, A14. doi: 10.1017/jfm.2019.826

Resing, J. A., Sedwick, P. N., German, C. R., Jenkins, W. J., Moffett, J. W., Sohst, B. M., & Tagliabue, A. (2015). Basin-scale transport of hydrothermal dissolved metals across the South Pacific Ocean. *Nature*, *523*(7559), 200–203. doi: 10.1038/nature14577

Rona, P. A., Klinkhammer, G., Nelsen, T., Trefry, J., & Elderfield, H. (1986). Black smokers, massive sulphides and vent biota at the Mid-Atlantic Ridge. *Nature*, *321*(6065), 33–37.

Rosso, I., Hogg, A. M., Kiss, A. E., & Gayen, B. (2015). Topographic influence on submesoscale dynamics in the Southern Ocean. *Geophysical Research Letters*, *42*(4), 1139–1147. doi: 10.1002/2014GL062720

Ruan, X., Si, Y., & Ferrari, R. (2025). Diapycnal upwelling driven by tidally induced mixing over steep topography. *Journal of Physical Oceanography*, *55*(3), 229–241. doi: 10.1175/JPO-D-24-0008.1

Saha, S., Moorthi, S., Pan, H.-L., Wu, X., Wang, J., Nadiga, S., ... others (2010). The NCEP climate forecast system reanalysis. *Bulletin of the American Meteorological Society*, *91*(8), 1015–1058. doi: 10.1175/2010BAMS3001.1

Sarrazin, J., Portail, M., Legrand, E., Cathalot, C., Laes, A., Lahaye, N., ... Husson, B. (2020). Endogenous versus exogenous factors: What matters for vent mussel communities? *Deep Sea Research Part I: Oceanographic Research Papers*, *160*, 103260. doi: 10.1016/j.dsr.2020.103260

Schifano, N., Vic, C., Gula, J., Molemaker, M. J., & McWilliams, J. C. (2025). Diapycnal mixing and tracer dispersion in a terrain-following coordinate model. *Journal of Advances in Modeling Earth Systems*, *17*(8), e2024MS004768. doi: 10.1029/2024MS004768

Shchepetkin, A., & McWilliams, J. (2005). The regional oceanic modeling system (ROMS): a split-explicit, free-surface, topography-following-coordinate oceanic model. *Ocean Modelling*, *9*(4), 347–404. doi: 10.1016/j.ocemod.2004.08.002

Tagliabue, A., Bopp, L., Dutay, J.-C., Bowie, A. R., Chever, F., Jean-Baptiste, P., ... others (2010). Hydrothermal contribution to the oceanic dissolved iron inventory. *Nature Geoscience*, *3*(4), 252–256. doi: 10.1038/NGEO818

Tagliabue, A., Lough, A. J., Vic, C., Roussenov, V., Gula, J., Lohan, M. C., ... Williams,

R. G. (2022). Mechanisms driving the dispersal of hydrothermal iron from the northern Mid Atlantic Ridge. *Geophysical Research Letters*, *49*. doi: 10.1029/2022GL100615

Tagliabue, A., & Resing, J. (2016). Impact of hydrothermalism on the ocean iron cycle. *Philosophical Transactions of the Royal Society A*, *374*(2081), 20150291. doi: 10.1098/rsta.2015.0291

Thakur, R., Arbic, B. K., Menemenlis, D., Momeni, K., Pan, Y., Peltier, W. R., ... Ma, Y. (2022). Impact of vertical mixing parameterizations on internal gravity wave spectra in regional ocean models. *Geophysical Research Letters*, *49*(16), e2022GL099614. doi: 10.1029/2022GL099614

Tuerena, R. E., Williams, R. G., Mahaffey, C., Vic, C., Green, J. M., Naveira Garabato, A., ... Sharples, J. (2019). Internal tides drive nutrient fluxes into the deep chlorophyll maximum over mid-ocean ridges. *Global Biogeochemical Cycles*, *33*, 995–1009. doi: 10.1029/2019GB006214

van Haren, H., Duineveld, G., & de Stigter, H. (2017). Prefrontal bore mixing. *Geophysical Research Letters*, *44*(18), 9408–9415. doi: 10.1002/2017GL074384

van Sebille, E., Griffies, S. M., Abernathey, R., Adams, T. P., Berloff, P., Biastoch, A., ... others (2018). Lagrangian ocean analysis: Fundamentals and practices. *Ocean modelling*, *121*, 49–75.

Vic, C., & Ferron, B. (2023). Observed structure of an internal tide beam over the Mid-Atlantic Ridge. *Journal of Geophysical Research: Oceans*, *128*(7), e2022JC019509. doi: 10.1029/2022JC019509

Vic, C., Gula, J., Roullet, G., & Pradillon, F. (2018). Dispersion of deep-sea hydrothermal vent effluents and larvae by submesoscale and tidal currents. *Deep-Sea Research Part I*, *133*, 1–18. doi: 10.1016/j.dsr.2018.01.001

Vic, C., Naveira Garabato, A. C., Green, J. M., Waterhouse, A. F., Zhao, Z., Melet, A., ... Stephenson, G. R. (2019). Deep-ocean mixing driven by small-scale internal tides. *Nature Communications*, *10*. doi: 10.1038/s41467-019-10149-5

Wagner, P., Rühs, S., Schwarzkopf, F. U., Koszalka, I. M., & Biastoch, A. (2019). Can Lagrangian tracking simulate tracer spreading in a high-resolution ocean general circulation model? *Journal of Physical Oceanography*, *49*(5), 1141–1157. doi: 10.1175/JPO-D-18-0152.1

Waterhouse, A. F., MacKinnon, J. A., Nash, J. D., Alford, M. H., Kunze, E., Simmons, H. L., ... others (2014). Global patterns of diapycnal mixing from measurements of the turbulent dissipation rate. *Journal of Physical Oceanography*, *44*(7), 1854–1872. doi: 10.1175/JPO-D-13-0104.1

Winters, K. B. (2015). Tidally driven mixing and dissipation in the stratified boundary layer above steep submarine topography. *Geophysical Research Letters*, *42*(17), 7123–7130. doi: 10.1002/2015GL064676